



Politecnico di Bari

Repository Istituzionale dei Prodotti della Ricerca del Politecnico di Bari

Determination of interfacial heat transfer coefficients in a sand mould casting process using an optimised inverse analysis

This is a pre-print of the following article

Original Citation:

Determination of interfacial heat transfer coefficients in a sand mould casting process using an optimised inverse analysis / Palumbo, Gianfranco; Piglionico, Vito; Piccininni, Antonio; Guglielmi, Pasquale; Sorgente, Donato; Tricarico, Luigi. - In: APPLIED THERMAL ENGINEERING. - ISSN 1359-4311. - 78:(2015), pp. 682-694.
[10.1016/j.applthermaleng.2014.11.046]

Availability:

This version is available at <http://hdl.handle.net/11589/1367> since: 2021-03-15

Published version

DOI:10.1016/j.applthermaleng.2014.11.046

Terms of use:

(Article begins on next page)

Determination of interfacial Heat Transfer Coefficients in a sand mould casting process using an optimized inverse analysis

G.Palumbo^{1, a}, V.Piglionico^{1, b}, A.Piccininni^{1, c}, P.Guglielmi^{1, d}, D.Sorgente^{1, e}
and L. Tricarico^{1, f}

¹Department of Mechanics, Mathematics and Management – Politecnico di Bari, viale Japigia 182
– Bari, Italy

^ag.palumbo@poliba.it, ^bvito.piglionico@poliba.it, ^cantonio.piccininni@poliba.it,
^dpasquale.guglielmi@poliba.it, ^ed.sorgente@poliba.it, ^ftricarico@poliba.it

Abstract

The determination of the interface heat transfer coefficients in casting processes represents a fundamental step in order to create a reliable numerical model able to predict some of the most common defects (for example hot tear or residual stress) which may affect the quality of the component. This work focuses the attention on the methodology to determine the heat transfer coefficients for the numerical modelling of the casting process of a superduplex stainless steel (ASTM A890 Gr. 5A) using a silica sand mould.

Experimental instrumented castings were used for acquiring by means of thermocouples (both in the casting and in the sand) the temperature evolutions in a certain number of points; in addition, the entire process was simulated adopting the finite difference method based commercial software package MAGMASOFT® (v. 5.2) in order to calculate the temperature distribution in the same points at any step of the process.

The most influencing input parameters were firstly chosen in order to determine the factors to be investigated using a reduced factorial scheme. Further simulations changing the value of the chosen factors allowed to plot as response surfaces the value of the misfit between experimental and numerical temperature evolutions in the same points.

The optimization procedure using a multi-objective genetic algorithm was thus adopted being the goal to find optimal values of the input parameters able to minimize the misfit between experimental and numerical temperature evolutions.

As confirmed by the numerical simulations using the results of the optimization procedure, the proposed methodology allowed to determine the proper values of the input variables for modelling the casting process of the ASTM A890 Gr.5A.

Keywords: Superduplex stainless steel (ASTM A890 Gr5A), Casting, MAGMASoft, interface Heat Transfer Coefficients, Response Surface, Multi Objective Genetic Algorithm.

1. Introduction

Duplex and Super Duplex Stainless Steels (DSS and SDSS) are characterized by a biphasic austenitic–ferritic microstructure (in balanced weight percentage) which ensures higher mechanical properties and stress corrosion resistance than the conventional austenitic stainless steels [1]. The difference between the DSS and SDSS can be resumed in the value of a representative parameter, the Pitting Resistance Equivalent Number (PREN), which is a function of the chemical composition of the alloy: SS with a PREN equal or greater than 40 can be classified as SDSS [2].

The above mentioned corrosion resistance properties make such alloys really attractive for several applications, such as: chemical, petrochemical, off-shore, chemical tankers, pulp and paper industry, pollution control equipment, desalination, sea-water applications [3].

In most of the above mentioned applications, DSS and SDSS components are manufactured by casting processes and it is fundamental to avoid the presence of defects like micro and macro porosity, hot tears, residual stresses and, of course, cracks.

A big contribution toward this goal can be given by the simulation: a numerical model can be used for simulating the whole casting process and predict the occurrence of the above mentioned defects; such an approach has clearly to rely on an accurate modelling of the thermo – physical properties of the specific alloy. In addition, the thermal boundary conditions must be correctly modelled, since the interface between the casting and the mould reveals to be the most crucial aspect in such kind of problems: in fact, interface Heat Transfer Coefficients (iHTC) strongly affect the thermal fluxes, but their evaluation is not always simple since several factors play a decisive role (casting geometry, pouring temperature, alloy and sand compositions, roughness, contact pressure, air gap, initial sand mold temperature, etc.). The necessary step of the iHTCs evaluation can be achieved adopting different methodologies: several authors proposed direct measurements [4-5] based on the immersion method, the fluidity test, the unidirectional test and the one-dimensional solidification process. Alternatively, an inverse analysis can be used: the experimentally measured temperatures become the target towards which the simulation has to be driven; the superimposition of the numerical and experimental temperature evolution can be reached calibrating the iHTC in the proper way [6-8].

Quite often the correct calibration of these coefficients is performed adopting various optimization algorithms: some authors adopted neural networks obtaining good accordance between numerical and experimental results even if the procedure revealed to be time consuming and needed high computational resources [9]. In fact, the determination of the iHTC is not always easy to reach since, in the solid-liquid region over the solidus curve, the temperature evolution is not only dependent on the heat transfer coefficients but also on other important variables (such as the thermal conductivity of the sand mould) [10].

In this work the authors focus the attention on the inverse analysis methodology and use the multi-objective genetic algorithm for the determination of the iHTC which characterize the thermal contact between the superduplex stainless steel ASTM A890 Gr.5A and the silica sand: at first reliable Response Surfaces were constructed on the base of results coming from a reduced factorial plan of numerical simulations.

2. Thermo-physical properties of the investigated materials

The chemical composition of the alloy ASTM A890 Gr. 5A is detailed in Table 1.

Table 1. Chemical Composition of the investigated alloy (ASMT A 890 GR.5A)

C	Si	Mn	Cr	Ni	Mo	P	N
0.024%	0.49%	0.74%	25.06%	7%	4.5%	0.02%	0.21%

Thermo-physical properties of the investigated alloy were determined in the labs of the CSM (Rome) by means of experimental tests. Density value at room temperature was calculated applying the Archimede's law on three specimens, obtaining an average value equal to 7.79 g/cm³; the other values (with respect to the temperature) were obtained from the experimental determination of the linear expansion coefficient (Figure 1a).

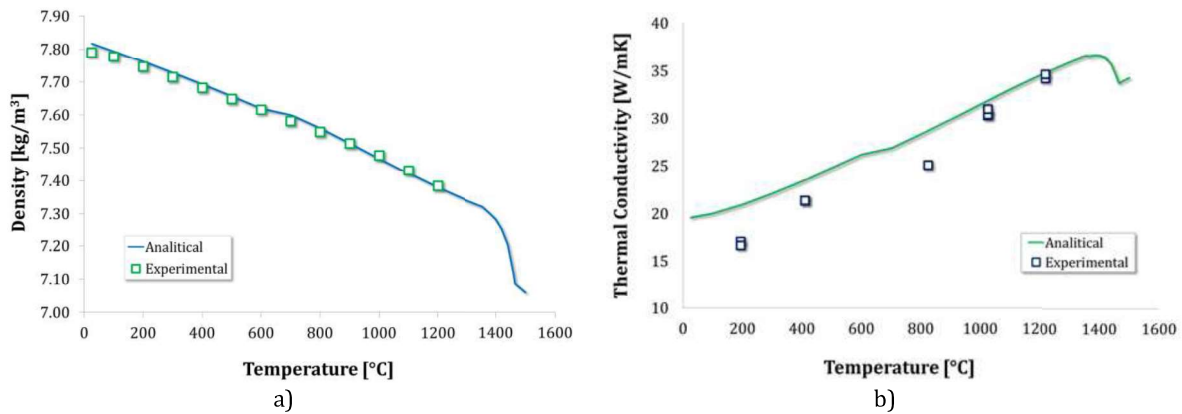


Figure 1. Experimental evaluation of the thermo-physical properties: a) density, b) thermal conductivity

Measurements of the thermal diffusivity (as a function of the temperature), which is the capability of the material to conduct the thermal energy, were used to calculate the thermal conductivity (Figure 1b) according to equation (1):

$$k = \alpha * \rho * c_p \quad (1)$$

where α is the thermal diffusivity, ρ and c_p represent the density and the specific heat respectively.

The same thermo-physical properties were also calculated using the CALPHAD (CALculation of PHase Diagrams) software JMatPro: as shown in Figure 1 (a, b), such numerical values revealed to be in good accordance with the experimental results, thus allowing to cover a wider temperature range.

In order to determine the melting range (liquidus and solidus temperatures) by means of a Differential Thermal Analysis (DTA), the specimen was heated in an oven; both the specimen and the oven chamber were equipped with thermocouples so that an accurate monitoring of temperature was possible. When the phase change occurred, a variation in the temperature evolution (shown in Figure 2a) was observed: the starting and the ending points of this variation can be linked to the solidus and liquidus temperatures (Figure 2b)

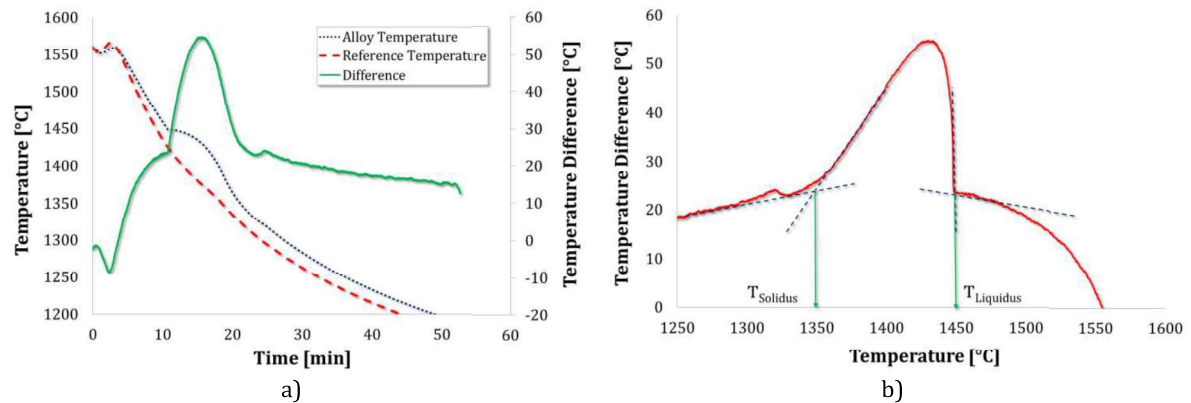


Figure 2. a) DTA output, b) Evaluation of Liquidus and Solidus temperatures.

Results of the analysis are detailed in Table 2; the analytically obtained liquidus and solidus temperatures were comparable to the correspondent experimental values.

Table 2. Liquidus and solidus temperatures of ASTM A 890 GR.5A.

$T_{\text{Liquidus}} [^{\circ}\text{C}]$	$T_{\text{Solidus}} [^{\circ}\text{C}]$
1447	1353

Since the heat transfer occurs between the alloy and the mould, also the thermal properties of the sand plays a relevant role: the thermal conductivity and the specific heat (C_p) as function of the temperature were thus experimentally determined.

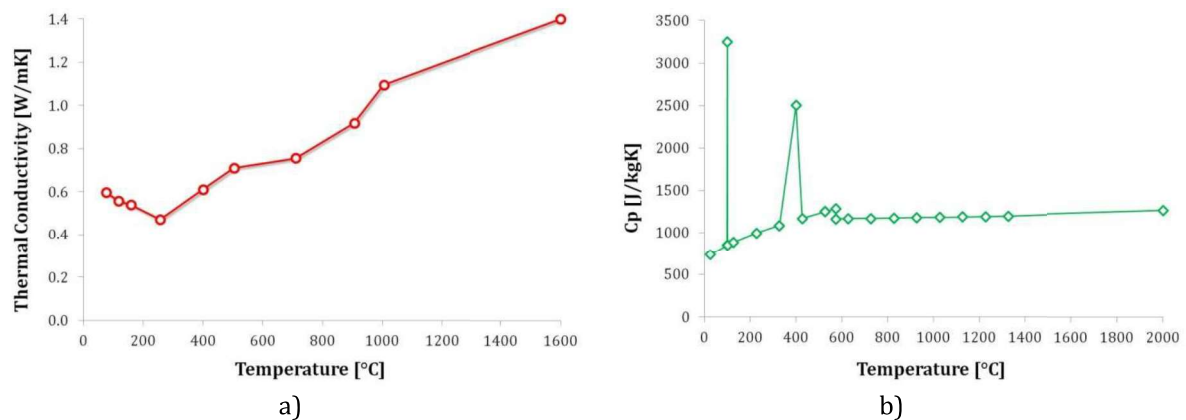


Figure 3. Thermo-physical properties of the silica sand: a) Thermal Conductivity; b) Specific heat

The thermal conductivity (Figure 3a) was evaluated using the same methodology adopted for the alloy, thus measuring the thermal diffusivity, the specific heat and the density; the thermal diffusivity, in turns, was obtained adopting a laser flash methodology (a pulsing laser beam hit the surface of the specimen and the temperature change on the opposite surface is recoded). As concerns the specific heat, Figure 3b shows that, in the range from room temperature to 1600°C, it is characterized by two peaks: the first one at 400°C (due to the binder combustion) and the second one (at about 100°C) due to the water vaporization.

3. Experimental set-up

Experimental instrumented castings, having the shape proposed in Figure 4 but changing the dimensions according to Table 3, were carried out.

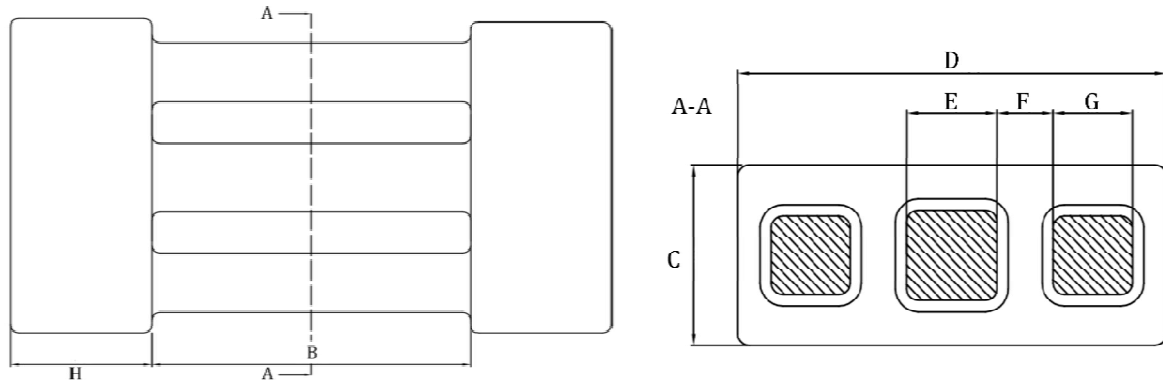


Figure 4. Experimental casting shape

Using two different geometries the robustness of the proposed methodology and of the obtained results was checked. In fact, different cooling rates could be determined and the correspondent effect on the temperature evolution was investigated.

Table 3. Main quotes of the two investigated geometries

Quote	Geometry A [mm]	Geometry B [mm]
B	200	180
C	80	80
D	200	190
E	60	40
F	20	25
G	35	35
H	80	80

The sand moulds creation was commissioned to the CSM (Rome): resin patterns made by selective laser sintering technique were used; one of the two halves of the resin pattern was drilled in order to create the holes for positioning the thermocouples (Figure 5). Temperature acquisitions were done adopting both B-type and K-type thermocouples monitoring the casting and the sand temperature evolution respectively: B-type thermocouples were positioned so that the junction could be placed in correspondence of the casting middle plane. As shown in Figure 5, the location of the thermocouples was defined in order to obtain temperature data about the massive regions at the two extremities of the part (yokes), about the central bar and about one of the side bars. On the contrary the K-type thermocouples were placed within the sand at a distance of 10 mm from the outer surface of the pattern.

The sand was finally compacted on a vibrational table and the pattern was removed after 15 minutes (it is related to the chemical reactions of the adopted phenolic resin binder).

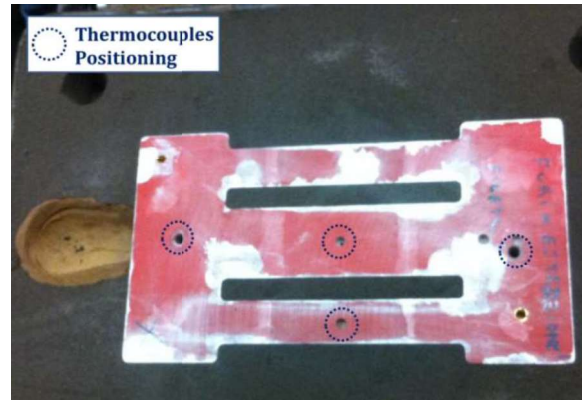
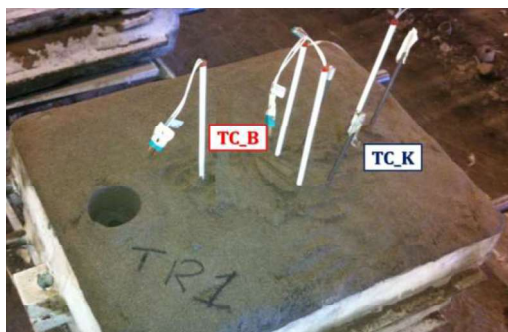


Figure 5. B type thermocouples positioning

After the completion of the compacting phase, the thermocouples were wired and subsequently connected to the acquisition system (Figure 6): the temperatures were acquired (frequency: 2 Hz) during the cooling until the shake out.



a)



b)

Figure 6. Instrumented mold: a) before pouring, b) during cooling

Experimental temperature data concerning the two geometries are plotted in Figure 7: it can be clearly noted the effect of the feeding modulus on the cooling rates of the middle points of the bars, as well as the time evolution of temperatures.

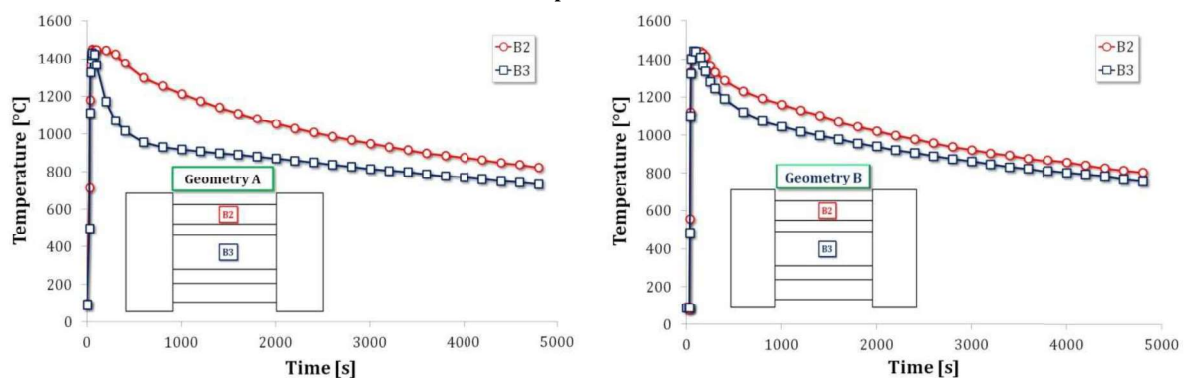


Figure 7. Temperature evolution: a) Geometry A, b) Geometry B

For each casting geometry, three replications were performed with the precise aim of demonstrating the repeatability of the acquisitions. As an example, the curves acquired by the B1 thermocouple (positioned within one of the two yokes) are reported in Figure 8.

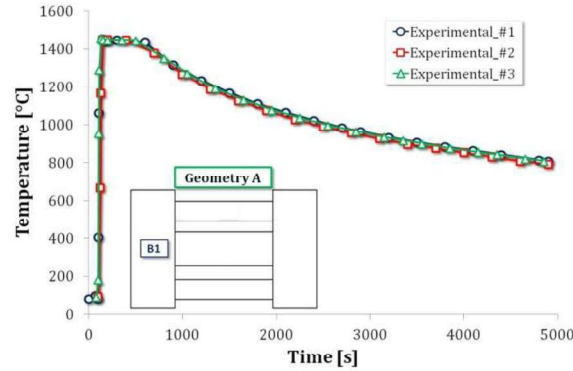


Figure 8. Comparison of the temperature evolution acquired by the thermocouple B1 positioned in the region of the yoke of the casting geometry A

It can be noted that temperature data are almost perfectly overlapped, thus confirming the highly repeatability of the acquisitions.

4. Description of the adopted methodology

From a theoretical point of view, the heat flux h across the interface between the metal casting and the sand mold can be described by the following equation (2):

$$h = \frac{\dot{q}}{T_c - T_s} \quad (2)$$

where \dot{q} is the average heat flux across the common interface, T_c and T_s are the evaluated temperature of the casting and the sand mould respectively.

On the other hand, the heat flow through the casting can be written according to the heat – transfer equation equation (3):

$$\nabla(k\nabla T) + q^* = \rho c \frac{\partial T}{\partial t} \quad (3)$$

where T is the temperature, t is the time, ρ is the density, c the specific heat, k is the thermal conductivity and q^* is a heat – source term. It can be expressed as a function of both the latent heat of solidification (l) and the solid fraction (f_s) according to equation (4):

$$q^* = \rho l \frac{\partial f_s}{\partial t} \quad (4)$$

Combining the previous two relations, equation 5 is obtained:

$$k \left[\frac{\partial^2 T(x,t)}{\partial x^2} + \frac{\partial^2 T(y,t)}{\partial y^2} + \frac{\partial^2 T(z,t)}{\partial z^2} \right] + \rho l \frac{\partial f_s}{\partial t} = \rho c \frac{\partial T}{\partial t} \quad (5)$$

Starting from this theoretical scenario, it is evident that the casting temperature evolution is strictly dependent from: (i) the heat transfer coefficients and (ii) the heat flow in the casting (that, in turns, is a function of both the latent heat and the solid fraction); in particular, a heat transfer coefficient that varies according to temperature is able to take into account the variation in the heat exchange due to the increasing air gap between the cast and the mold as the casting shrinks during cooling [4, 11].

Consequently, a proper set of input parameters has to be defined: the approach adopted by the authors was to run preliminary simulations in order to understand the most influencing quantities involved in the process.

Figure 9 shows the variation of the temperature evolution obtained if increasing (about 15%) the values of the middle points which define the solid fraction profile over the solidification temperature range.

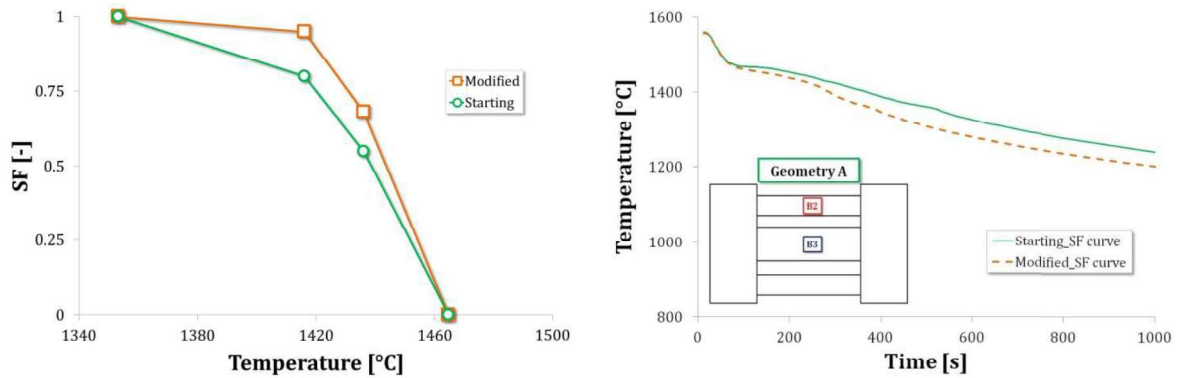


Figure 9. Solid fraction effect on the temperature distribution in the higher temperature zone

From the analysis of Figure 9, the influence of such a parameter on the temperature evolution appears evident, especially in the range immediately after the material solidification. A similar effect was produced when changing the parameter l (latent heat), which had an influence on the temperature distribution in the region of the highest temperatures.

According to this, beside the iHTC, the solid fraction and the latent heat were included in the list of parameters to be evaluated using the inverse methodology approach.

In order to easily vary, also using a Design of Experiments scheme, both the solid fraction and the iHTC curves (the value of such parameters changes according to temperature thus defining a curve over the temperature range), they were simplified using a reduced number of points as shown in Figure 10: in order to vary the solid fraction curve, two of the four points (SF#2 and SF#3) were changed (Figure 10a); in order to change the iHTC curves, three points (HTC#1, HTC#2 and HTC#3) were changed and thus considered as input parameters (Figure 10b). On the contrary, the parameter latent heat was simply varied in the range 100 – 160 [kJ/kg].

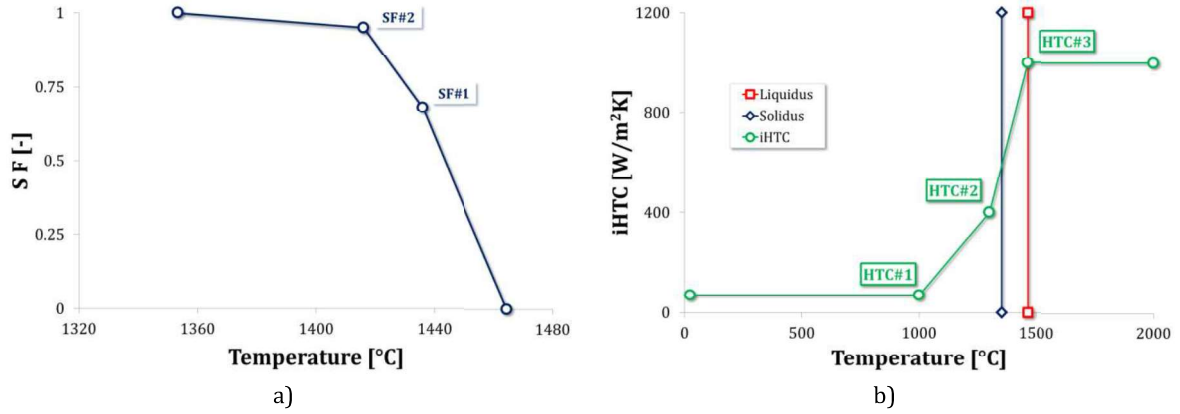


Figure 10. a) Solid Fraction and b) iHTC as function of temperature

Values of the investigated factors were defined according to a reduced factorial scheme (32 runs): upper and lower value for each of the considered input parameter are reported in Table 4.

Table 4. Range of variation of the input variables

Input Variable	Value	
SF#2	Upper Value	0.98
	Lower Value	0.8
SF#1	Upper Value	0.7
	Lower Value	0.5
HTC#1 [W/m²K]	Upper Value	50
	Lower Value	200
HTC#2 [W/m²K]	Upper Value	300
	Lower Value	700
HTC#3 [W/m²K]	Upper Value	800
	Lower Value	1200
LH [kJ/kg]	Upper Value	100
	Lower Value	160

The fitting between the numerical and the experimental temperature fields was evaluated comparing numerical and experimental temperature evolutions measured by thermocouples (acquisition frequency: 1/25 Hz). The following error function, according to equation (6), was thus defined and used for estimating the ability of the set of the input parameters to catch the real temperature evolution:

$$\text{Err_TC} = \sum_{t=25}^{4800} (T_{\text{num}} - T_{\text{exp}})^2 \quad (6)$$

where T_{num} and T_{exp} are respectively the numerical and the experimental temperature at a certain time point, 25 is the first time point considered and 4800 is the last time point (just before the shake – out).

The objective function was calculated for all thermocouples, both B and K type, thus assuming the name according to the number and the type of the Thermocouple (*Err_K1*, *Err_K2*, *Err_B1*, etc.). Each objective function was assumed as an output variable and all of them were used for transforming the results of the simulations into a set of data available for the response surfaces methodology and for the optimization procedure detailed in the following sections.

5. Numerical modeling of the casting process

Simulations were carried out using MAGMASoft (v. 5.2) [12]. In Figure 11 (a,b) the entire casting entity (the component and the gating system) is shown, highlighting the position of the adopted virtual thermocouples which were defined in the same points where real thermocouples in the instrumented casting experiments were positioned. The MAGMA model, including all the generated volumes (the casting, the sand mould and the gating system) is shown in Figure 11c.

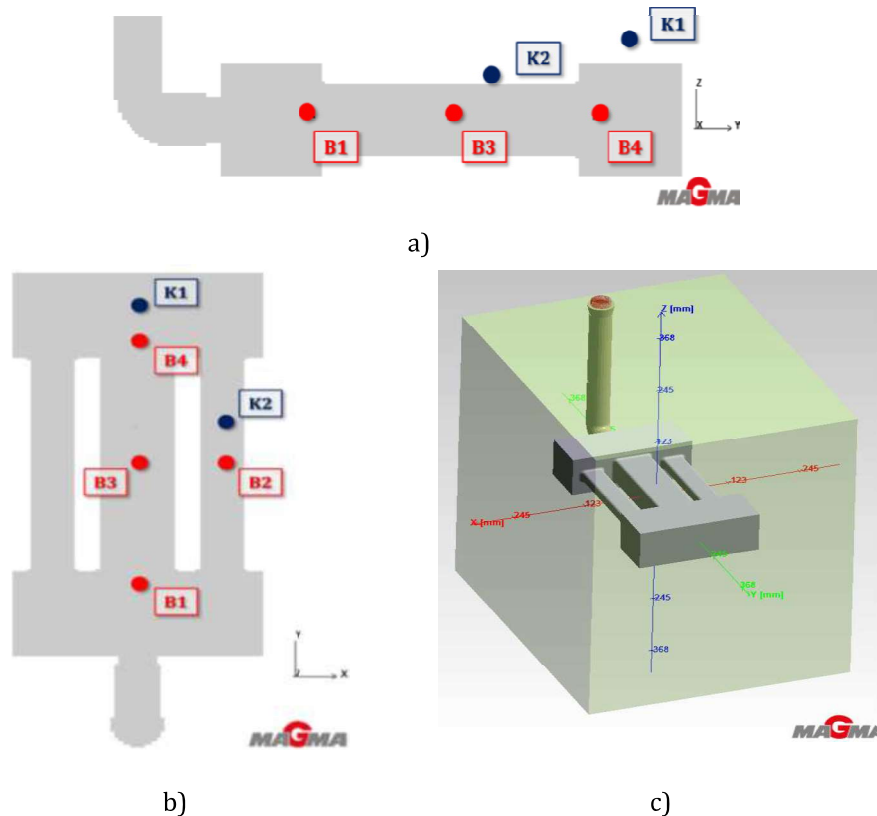


Figure 11. Virtual thermocouple positioning: a) lateral view, b) top view and c) geometry modeling

In particular, Table 5 resumes the exact positions for all thermocouples in terms of coordinates in the reference system whose origin is placed at the casting center of mass (B3 position).

Table 5. Thermocouples positions

TC	X [mm]	Y [mm]	Z [mm]
B1	0	-115	0
B2	69.2	0	0
B3	0	0	0
B4	0	115	0
K1	0	152	51
K2	69.2	37	20.25

The adopted mesh was characterized by 2.000.000 elements (256.524 metal cells). In order to reduce computational costs the pouring step was neglected, thus taking into account only the solidification and cooling phases, assuming the temperature of 1560°C (it is the measured ladle temperature before pouring) as the initial temperature.

6. Response Surface Methodology (RSM)

In order to minimize the error functions created according to equation (6), an optimization procedure developed in the commercial software modeFRONTIER® (v. 4.5.3) environment was used. According to the workflow scheme presented in Figure 12, each variable belonging to the group of the output variables is connected to an objective function; the DoE node in the middle zone, which manages the optimization procedure as specified in the following section 7, collects the data coming from the groups on both the left side (the input variables) and the right side (the output variables).

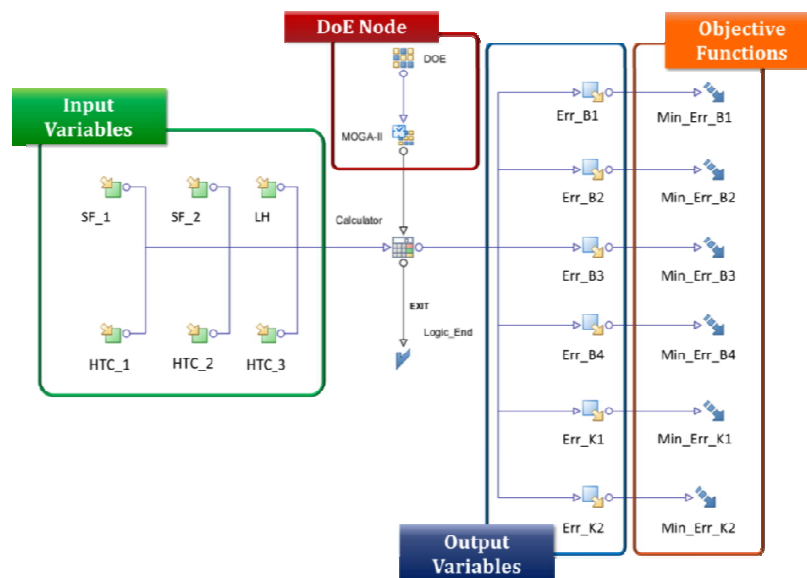


Figure 12. Workflow of the optimization procedure created in the modeFRONTIER environment

For each of the above described output variable a Response Surface (RS) was built adopting the Radial Basis Function algorithms available within the modeFRONTIER environment. Radial Basis Functions represent a powerful tool for interpolating scattered data: in general, starting data do not need to be sampled on a regular grid (Radial Basis Functions are usually defined as “meshless” interpolating functions). In addition, such functions allow to create interpolant response surfaces, since the points of the starting dataset surely belongs to the surface [13]. Starting from n points belonging to the function $f(x)$ (where $f(x_i) = f_i$ are the n points to be fitted by the RS) an interpolant RBF can be analytically defined according to the following equation 7:

$$s(x) = \sum_{j=1}^n c_j \phi(\|x - x_j\|/\delta) \quad (7)$$

where $\|\cdot\|$ is the Euclidean norm, δ is a fixed scaling parameter and $\phi(r)$ is the radial function. The coefficient c_j are defined “free parameters” and they can be obtained imposing the interpolation equations. The five algorithms available in the modeFRONTIER environment for creating a Radial Basis Function RS are detailed in Table 6.

Table 6. Types of Radial Basis Functions available within the modeFRONTIER environment

Name	Analytical expression
Gaussian (G)	$\phi(r) = \exp(-r^2)$
Duchon's Polyharmonic Splines (PS)	$\begin{aligned} \phi(r) &= r^3 & d \text{ odd} \\ \phi(r) &= r^2 \log(r) & d \text{ even} \end{aligned}$
Hardy's MultiQuadratics (HMQ)	$\phi(r) = (1 + r^2)^{\frac{1}{2}}$
Inverse MultiQuadratics (IMQ)	$\phi(r) = (1 + r^2)^{(-\frac{1}{2})}$
Wendland's Compactly Supported (W2)	$\begin{aligned} \phi(r) &= (1 - r)^3 + (3r + 1) & d = 1 \\ \phi(r) &= (1 - r)^4 + (4r + 1) & d = 2, 3 \\ \phi(r) &= (1 - r)^5 + (5r + 1) & d = 4, 5 \end{aligned}$

A good rule in order to check the accuracy of an interpolant RS is to evaluate the *Mean Leave One Out Error* (MLOOE): in turn, each point belonging to the training set is excluded from the training procedure; the value predicted in the excluded point by the resulting surface is then compared to the known value. The leading idea is that the smaller this value, the better the surface is trained on the whole dataset. If the MLOOE is below 0.2 a good fitting is ensured. A severe drawback of this technique, which often prevents its adoption, is the huge computational cost: n different surfaces have to be created, each using $n-1$ training points, being n is the size of the original training set.

Another important parameter which can be checked is the *Scaling Parameter* (SP), which has a decisive influence on the shape of the Radial Basis Function: a too low SP value leads to narrow peaks at the training points, while too high values cause an excessive smoothing of the

surface that consequently is not completely able to interpolate the training points. The total amount of data coming from simulations was thus divided into two groups: the training set (assumed to be about 90% of the entire set) for the preliminary training of the RSs and the validation set (assumed to be the remaining 10%) on which the capability of fitting results was evaluated.

In order to optimize the selection of the radial basis function algorithm to be used for creating response surfaces able to fit numerical results, after the training step the RS fitting capability was evaluated checking both the MLOOE and the residuals calculated on the designs composing the validation set. As an example, in the following the procedure concerning the RS of the output variable *Err_B1* is described. The most reliable response surfaces after the training resulted the ones obtained using the Hardy's MultiQuadrics (HMQ), the Inverse MultiQuadrics (IMQ) and the Gaussians (G) algorithms. But analyzing both the MLOOE values and the residuals (as validation set data coming from simulations #17, #29 and #30 were used) in Figure 13, none of the three could be immediately chosen as the best since differences can be considered negligible.

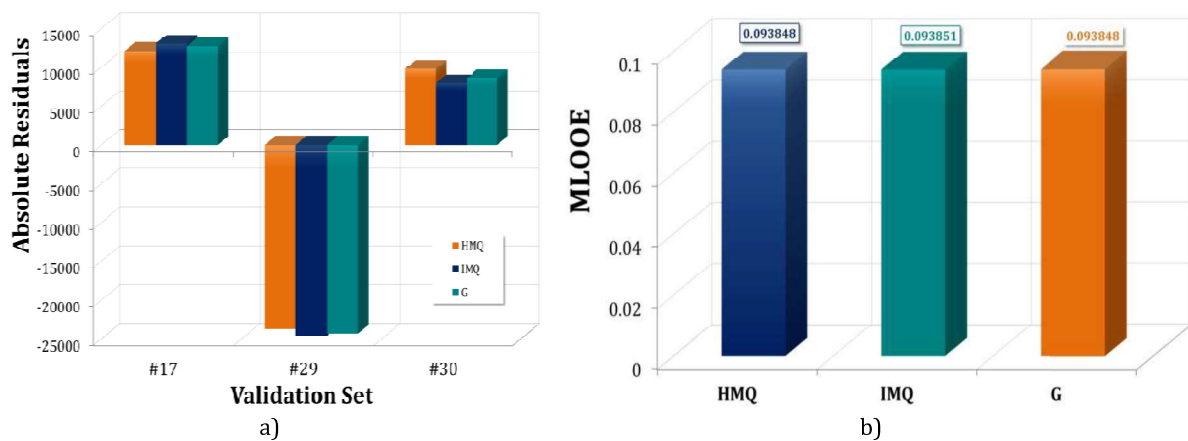


Figure 13. Evaluation of the fitting capability of the RS concerning *Err_B1*: a) residuals on validation set, b) MLOOE

The approach followed for solving the problem was to analyze the surfaces plotting them contemporarily on common (two-dimensional) graphs, thus creating one graph for each variable (Function Plot): again, as an example, in Figure 14 are reported the 6 Function Plots concerning the *Err_B1* output variable. Since the output variable has to be minimized by the optimization procedure, the criterion adopted by the authors for choosing as the best RS was to overestimate its maximum value. As shown in the example reported in Figure 14, the RS obtained applying the Gaussians algorithm (symbol: triangles) was positioned above the other curves and this made this RS be preferable for the subsequent optimization.

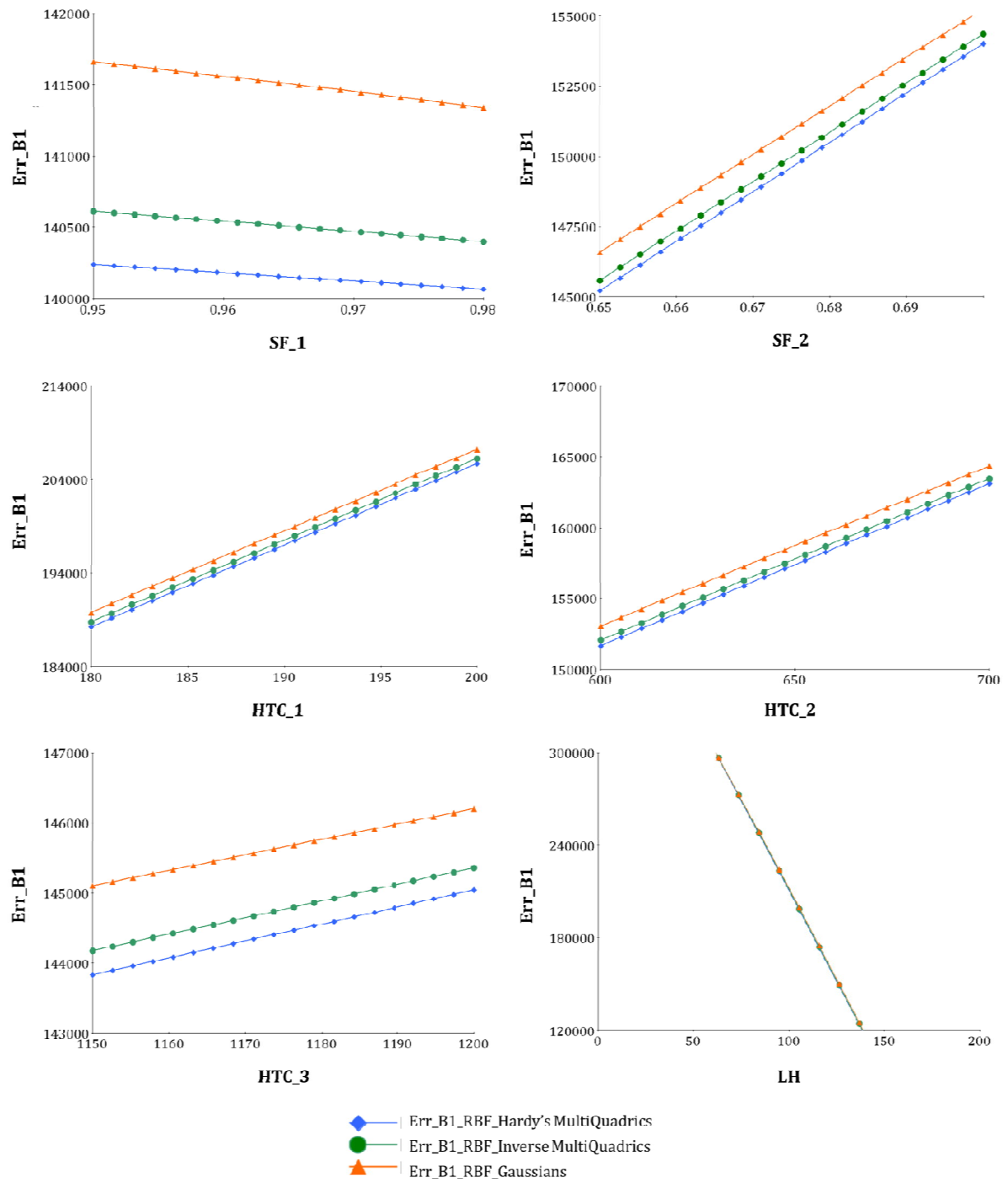


Figure 14. Function Plots concerning the output variable Err_B1

In order to determine the most reliable response surfaces, the above mentioned procedure was applied for each output variable. The Table 7 resumes the chosen algorithms and the fitting capabilities (simply in terms of MLOOE) for all the created response surfaces.

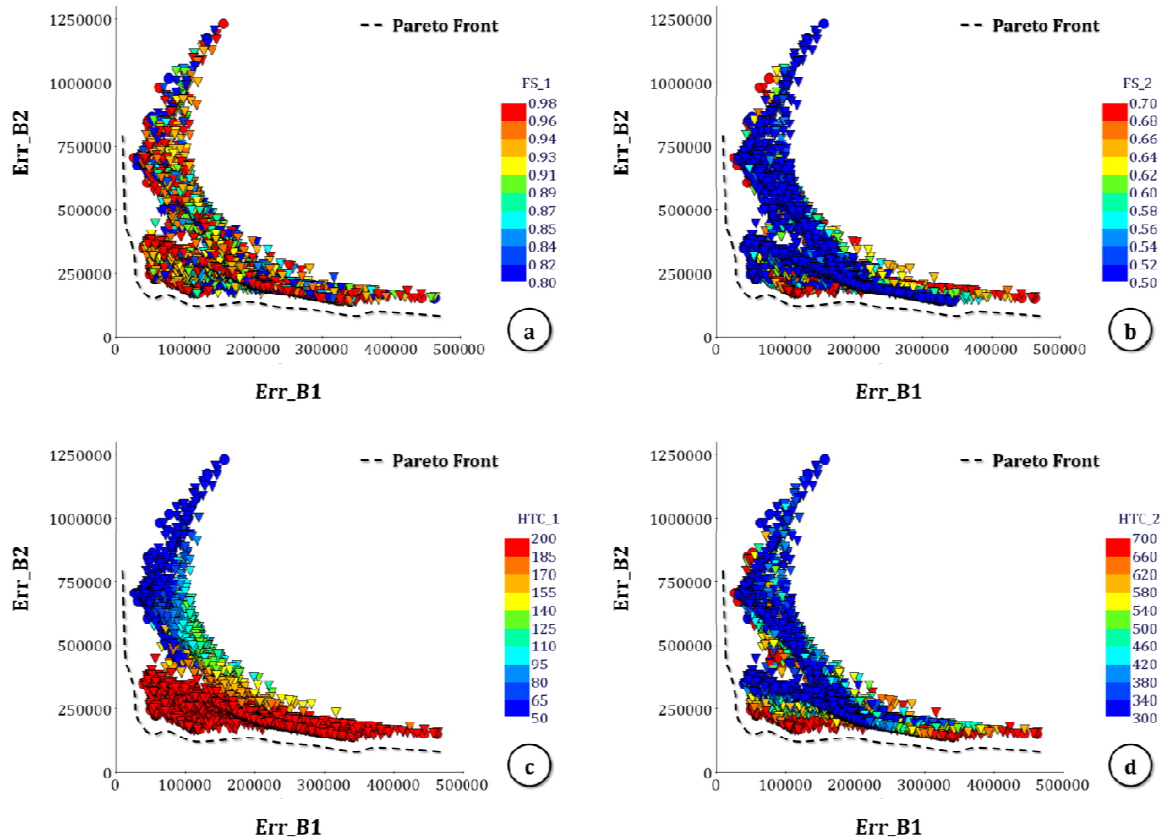
Table 7 Response Surfaces: Fitting capabilities and chosen algorithms

Output Variable	MLOOE	Chosen Algorithm
Err_B1	0.09385	Gaussians
Err_B2	0.04064	Gaussians
Err_B3	0.1283	Gaussians
Err_B4	0.07129	Gaussians
Err_K1	0.20	Gaussians
Err_K2	0.01750	Inverse MultiQuadratics

7. Optimization procedure

The purpose of the optimization procedure was to minimize the error between the numerical and the experimental temperature evolution in all investigated points. In order to perform such an optimization, an initial population of 75 virtual designs was created on the base of the initial data set adopting a space filler algorithm able to avoid design clusters.

As optimizing algorithm the MOGA-II (an improved version of the Multi-Objective Genetic Algorithm) was adopted, setting the number of successive generations to 100. Such an algorithm uses a smart multisearch elitism for robustness and directional crossover for fast convergence, combined with different operators (classical crossover, mutation and selection) [14]. Bubble charts in Figure 15 show the evolution of the optimization procedure: the set of optimal virtual designs represent the Pareto front (dashed curve in each bubble chart).



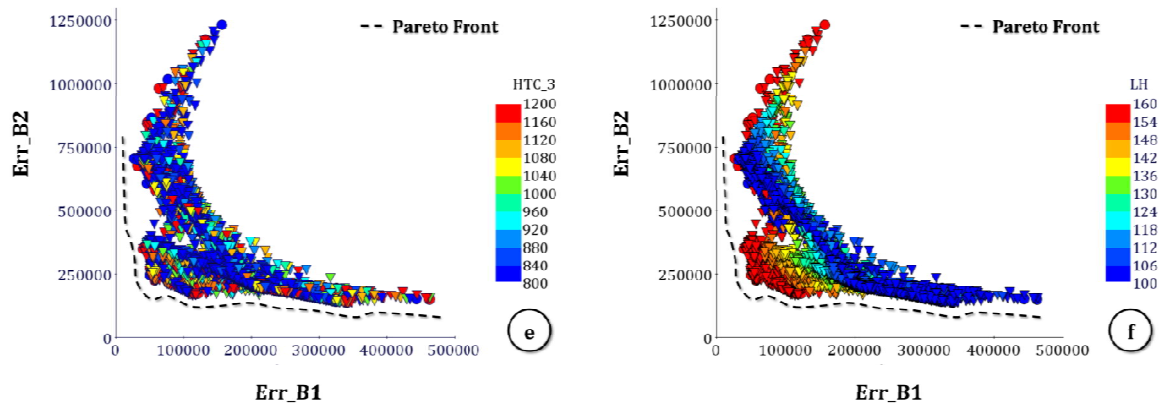


Figure 15. Optimization results: bubble charts

Since the optimization procedure gave back a high number of potentially virtual optimal solutions, final values of the input parameters were determined averaging the input values corresponding to the optimal designs.

Table 8. Final values of the input variable determined using the optimization procedure

Input Variable	Optimal Average Value
SF#1	0.52
SF#2	0.92
HTC#1 [W/m ² K]	194
HTC#2 [W/m ² K]	360
HTC#3 [W/m ² K]	905
LH [kJ/kg]	110

In Table 8 the final values determined using the optimization procedure are listed, while in Figure 16 the resulting solid fraction curve (a) and iHTC curve (b) are shown. In the same figure also the starting curves available in literature [15] are plotted.

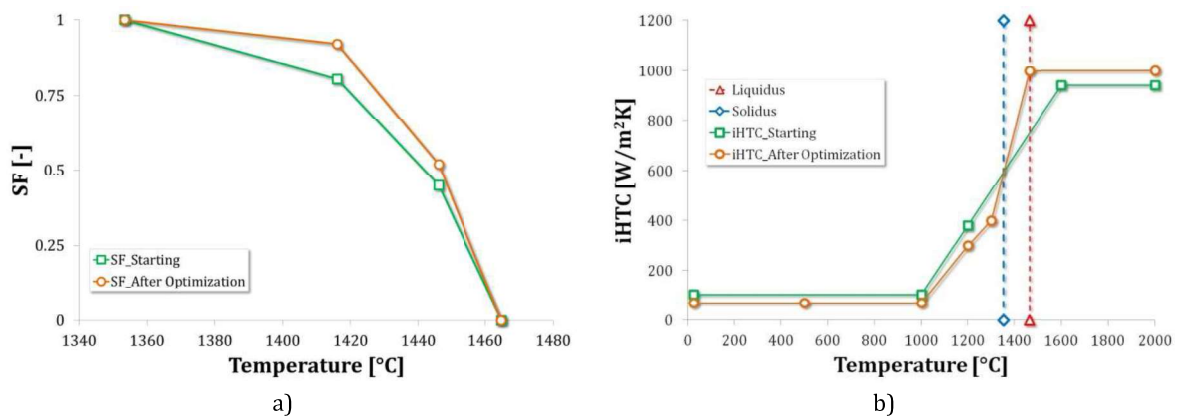


Figure 16. Results of the optimization procedure: a) solid fraction curve; b) iHTC curve

Results coming from the optimization are useful to understand how the input parameters affect the adopted output variables. If considering the latent heat, setting its value at the minimum of the investigated range determines an increase of the Err_B1 value, thus meaning that the fitting of the experimental by the numerical one becomes worse.

If considering the iHTC values, too low values of the HTC#1 causes an increasing value of the Err_B2 output variable since a low value in the heat transfer coefficient reflects in higher numerical values than the ones experimentally acquired.

It is also important to highlight that the correct modeling of the temperature effect on both the iHTC and the solid fraction appears to be fundamental for the simulation of the process. In particular, if considering the solid fraction, the implementation of the correct curve is useful for accurately reproducing the thermal history in the region of the highest temperatures, where most of the common defects originates and thus the capability of catching the real material behavior plays a key role.

Results of the optimization procedure were directly implemented within the numerical model: further numerical simulations were run adopting the values of the input parameters evaluated by the proposed methodology. In this last simulation the pouring phase was taken into account considering an interval of 13 seconds to fill the whole sand mold (the same used in the casting experiments).

Results are presented in Figure 17 in terms of temperature evolutions acquired by thermocouples (continuous red curves), obtained by the numerical model when the starting value of the iHTC were implemented (dotted green curves) and obtained by the numerical model when applying the final values proposed by the authors (dashed blue curves).

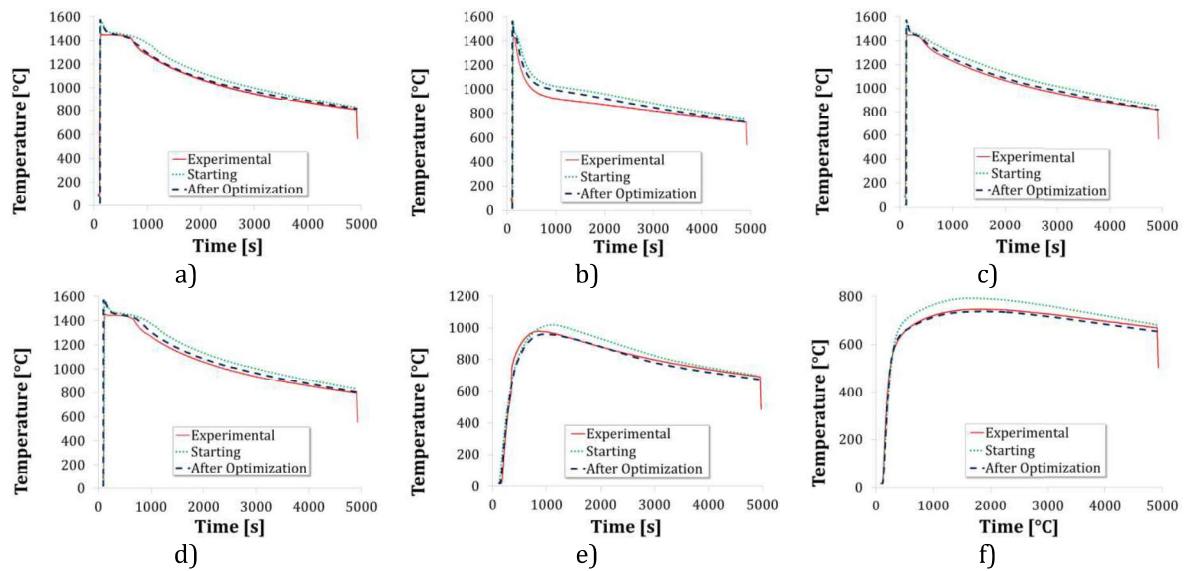


Figure 17 Comparison of temperature evolution: a) B1, b) B2, c) B3, d) B4, e) K1, f) K2

Focusing the attention at temperature trends of the B-type thermocouples, it is possible to note the presence of an initial peak in the high temperature region, while the experimental acquisition exhibited a smoother behavior as also documented in other works [16]: this difference is due to the fact that the thermocouples adopted in the experimental tests were

equipped with a ceramic sheath, while the virtual thermocouples behave like a bare wire type. As a further proof of the reliability of the optimization results, the obtained optimal values of the input parameters were also used for simulating the casting geometry B. The numerical and experimental temperature evolutions shown in Figure 18 are also in this case perfectly overlapped.

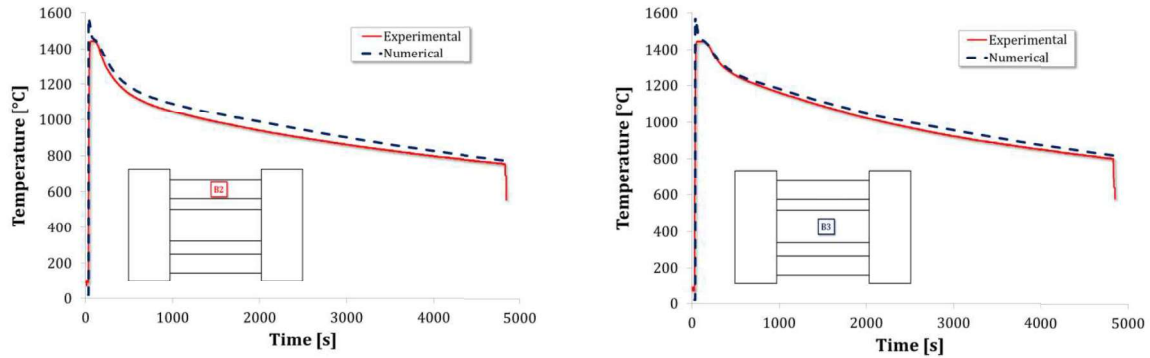


Figure 18 Verification of the optimized input parameters on the Geometry B

8. Conclusions

In order to perform robust numerical simulations for the investigation of sand casting processes, the modeling of heat transfer phenomena, especially in the range of elevated temperature where main casting defect originates (hot tears, residual stresses due to plastic strain under the effect of thermal stresses, porosity) needs to be accurate.

According to preliminary simulations and as confirmed by literature, it involves not only the evaluation of the interfacial heat transfer coefficients, but also the thermo – physical properties of the materials (both the alloy and the sand constituting the mould). In addition, the majority of the parameters affecting the specific thermal interaction between the materials involved in the heat transfer phenomena are temperature dependent and the adoption of an averaged value represents a rough approximation.

The numerical/experimental methodology proposed by the authors allows to determine, as function of the temperature, the most important parameters able to fully catch the heat transfer phenomena of a sand casting process; as case study, the superduplex stainless steel ASTM A890 Gr5A was considered in the present work.

In particular, using the proposed optimization procedure aimed to minimize the misfit between the calculated numerical temperature evolutions and the experimental ones acquired by thermocouples (function Err_TC), the curves representing the variation (due to the temperature) of both the interfacial heat transfer coefficients and the solid fraction were successfully determined, together with an optimal value of the latent heat.

Despite the low number of initial simulation runs (designs) defined according to a reduced factorial plan, interpolant response surfaces revealed to be very accurate and able to correctly catch the effect of each factor on the output parameter.

The initial misfit between numerical temperature evolutions during cooling, calculated using data from literature as starting values for the interfacial heat transfer coefficients, the solid fraction and the latent heat, was effectively reduced at the end of the optimization procedure. The effectiveness and the robustness of the proposed methodology, together with the accuracy and the fitting capability of the adopted response surfaces, was confirmed by the simulation of two different casting geometries: if setting the investigated parameters at the final values, both presented an optimal fitting between experimental and numerical temperature fields.

The proposed methodology is valid for any material and any process, being fast and easily manageable with conventional computational resources. In addition, results can be further refined increasing the number of control points which define the curve representing the parameter variation with respect to the temperature.

Acknowledgments

The authors wish to thank Dr. R. Sorci and Dr. G. De Rosa (CSM, Rome) for their contribution in the experimental activity. The activities in this work were funded by the Italian Government in the framework of the European National Operative Programme for Research and Competitiveness (project acronym: SMATI).

References

- [1] Tavares SSM, Silva VG, Pardal JM, Corte JS. Investigation of stress corrosion cracks in a UNS S32750 superduplex stainless steel. *Eng Fail Anal* 2013; 35:88-94.
- [2] Mc Guire MF. *Stainless Steels for Design Engineers*. 1st ed.: ASM International; 2008.
- [3] Charles J. Duplex Stainless Steel, a review after DSS 07 held in GRADO. *Revue de Métallurgie* 105 (2008) 155-171.
- [4] Nishidam Y, Droste W, Engler S. The air-gap formation process at the casting-mold interface and the heat transfer mechanism through the gap. *Metall Mater Trans B* 1986; 17:833-44.
- [5] Prates M, Biloni H. Variables affecting the nature of the chill zone. *Metall Mater Trans B* 1972; 3:1501-10.
- [6] Sun Z, Hu H, Niu X. Determination of heat transfer coefficients by extrapolation and numerical inverse methods in squeeze casting of magnesium alloy AM60. *J Mater Process Tech* 2011; 211:1432-40.
- [7] Zhang W, Xie G, Zhang D. Application of an optimization method and experiment in inverse determination of interfacial heat transfer coefficients in the blade casting process. *Exp Therm Fluid Sci* 2010; 34:1068-76.
- [8] Dong Y, Bu K, Dou Y, Zhang D. Determination of the interfacial heat transfer coefficient during investment-casting process of single-crystal blades. *J Mater Process Tech* 2011; 211:2123-31.
- [9] Zhang L, Li L, Ju H, Zhu B. Inverse identification of interfacial heat transfer coefficient between the casting and mold using neural network. *Energ Convers Manage* 2010; 51:1898-04.

- [10] Wong MLD, Pao WKS. A genetic algorithm for optimizing gravity die casting's heat transfer coefficients. *Expert Syst Appl* 2011; 38:7076-80.
- [11] Vynnycky M. On the onset of air-gap formation in vertical continuous casting with superheat. *Int J Mech Sci* 2013; 73: 69-76.
- [12] MAGMASoft v. 5.2. Standard and Simulation of Steel Casting Manuals
- [13] Rigoni E. Radial Basis Functions Response Surfaces. ESTECO Technical Report 2007; modeFRONTIER User's Manual.
- [14] Poles S. MOGA-II An improved Multi-Objective Genetic Algorithm. ESTECO Technical Report 2003; modeFRONTIER User's Manual.
- [15] Baghani A, Davami P, Varaham N, Shabani MO. Investigation of the effect of mold constraint and cooling rate on residual stress during the sand-casting process of 1086 steel by employing a thermomechanical model. *Metall Mater Trans B* 2014; 45:1157-69.
- [16] Long A, Thornhill D, Armstrong C, Watson D. Determination of the heat transfer coefficient at the metal-die interface for high pressure die cast AlSi9Cu3Fe. *Appl Therm Eng* 2011; 31:3996-06.